

URANS PREDICTION OF THE SLAMMING COEFFICIENTS FOR PERFORATED PLATES DURING WATER ENTRY

(DOI No: 10.3940/rina.ijme.2018.a1.447)

W Zhang, S Chai, H Nguyen, and Y Jin, National Centre for Maritime Engineering and Hydrodynamics, Australian Maritime College, University of Tasmania, Australia

SUMMARY

The slamming coefficients for perforated plates of various perforation ratios and layout configurations were predicted using Unsteady Reynolds-Averaged Navier-Stokes (URANS) solver STAR-CCM+. The numerical model was validated by comparing with experimental measurements of slamming coefficient for a circular cylinder. The slamming coefficients and free surface profiles of perforated plates were then predicted at full-scale. It was found the air compressibility plays an important role by studying flat plate water entry phenomena. For perforated plates with small gap length/width ratios, the ability of the trapped air to evacuate through the space between the bottom of the plate and free surface is similar. For perforated plates with different gap number at a fixed perforation ratio, the slamming coefficient is increased with the increase in gap length/width ratio. However, a further increase in length/width ratio may impose a negative impact on the escape of trapped air due to the increase of gap number.

NOMENCLATURE

R	Radius of cylinder (cm)	ε_{k21}	differences between medium-fine solutions
V	Drop velocity (m/s)	S_{k3}	Coarse solution result
G_B	Mesh Base size (mm)	S_{k2}	Medium solution result
T	Temperature (°C)	S_{k1}	Fine solution result
Q	Volume energy sources	R_k	Convergence ratio
\mathbf{u}	Velocity field in Cartesian coordinates (m/s)	S_U	Maximum oscillation solution result
∇	$(\partial / \partial x, \partial / \partial y, \partial / \partial z)$	S_L	Minimum oscillation solution result
P	Pressure (N m ⁻²)	$\delta_{RE_{k1}}^*$	Numerical error
\mathbf{g}	Gravitational acceleration (m/s ²)	δ_{k1}^*	Numerical error if C_K is close to 1
ν	Kinematic viscosity (m ² /s)	P_k	Order of accuracy
ρ	Density (kg m ⁻³)	C_K	Correction factor
ρ_{air}	Density of air (kg m ⁻³)	P_{kest}	Limiting order of accuracy
ρ_{water}	Density of water (kg m ⁻³)	S_c	Benchmark value
μ	Dynamic viscosity (N s m ²)	U_{kc} / U_k	Grid, time-step or iterative uncertainty
μ_{air}	Dynamic viscosity of air (N s m ²)	C_S	Slamming coefficient
μ_{water}	Dynamic viscosity of water (N s m ²)	F_S	Force acting on the object in vertical direction (N)
e	Specific sensible energy (J/kg°C)	A_P	Project area of object normal to the direction of oscillation (m ²)
λ	Transport coefficient	v_S	Slamming impact velocity (m/s)
α_i	Volume fraction	DNV	Det Norske Veritas
$S\alpha_i$	Source of sink of each phase	VOF	Volume of Fluid
$D\rho_i / Dt$	Lagrangian derivative of the phase density	URANS	Reynolds-Averaged Navier-Stokes
U_{SN}	Numerical uncertainty		
U_I	Iterative uncertainty		
U_G	Grid uncertainty		
U_T	Time-step uncertainty		
r_k	Refinement ratio		
ε_{k32}	differences between coarse-medium solutions		

1. INTRODUCTION

In recent years, oil and gas companies are actively searching for oilfields in deeper waters. In comparison to shallow water marine operations, higher safety standards are essential, which require subsea structures to be lowered across the splash zone and installed safely. This is especially true for the subsea structures with large horizontal surfaces such as baseplates, mud mats and horizontal subsea trees

(Faltinsen, 1990). During the installation process, if the water impact load (i.e. slamming force) occurring within a short duration when a structure penetrates the water surface, is larger than the self-weight of subsea structure in air, a 'weightlessness' phenomenon will occur. This large impact force will result in hoisting line slack, which leads to a snap force thereafter. To avoid this situation and ensure a successful lowering operation, it is critical to estimate the slamming forces during the design process. DNV-RP-H103 (2011) provides a series of benchmark values for the slamming coefficients for simple objects, which includes cylinders and flat plates. However, the applicability of these recommended values is limited since subsea structures have become more complicated in terms of geometrical shapes and sizes (i.e. suction anchor) for deep water zone. In this paper, the object of interest is the perforated plate, which is an important component of typical subsea equipment, for example, a protection shell for the manifolds or a baseplate acting as a loading supporting device.

In the late of 1920's, Von Karman (1929) started studying the slamming problem analytically for a seaplane from the view of classical mechanics. He applied the law of conservation of momentum to determine the maximum pressure. However, many variables were neglected such as gravity, the compressibility of air and water; and especially the local uprise of water. Therefore, to consider the effect of the free surface, Wagner (1932) then introduced potential flow theory to describe this phenomenon. Based on his theory, the body wetted length contacting with the free surface is extended longer due to local uprise of water. Following these two analytical approaches for investigating a free-falling circular cylinder (Faltinsen, 1990), both of them are considered to have their limitations in predicting the slamming coefficients by comparing against the experimental results (Campbell and Weynberg, 1980). In addition, both Von Karman and Wagner's approaches are two-dimensional methods. Therefore, it is difficult to claim which approach will give a better result when considering three-dimensional effects, such as the gravity, side effect and air cushion. However, it should be pointed out that the Wagner's approach provides more details of the flow at the spray zone.

Numerous experiments have been performed in the last 50 years and the most widely studied tests are the free drop test and constant drop test. Verhagen (1967) and Chuang (1966, 1970) studied the air cushion effect, whereby the air trapped beneath the flat plate was observed during water entry while having wedges with a deadrise angle of less than 3°. They also found that the trapped air deformed the water surface. Which significantly reduced the expected maximum impact pressure as the air pocket was forced out from the bottom of the plate. Campbell and Weynberg (1980) conducted a constant drop test using a circular cylinder, and a formula was derived from the experimental data to calculate the slamming coefficients. A more recent experiment conducted by Huera-Huarte *et al.* (2011) showed that asymptotic theory could predict loading on the flat plate

well, only when the deadrise angle is larger than 5°. This proves that air compressibility plays an important role especially in areas where the deadrise angle is very small. In addition, they also reported that the slamming coefficient is strongly related to the impact velocity. These experimental results are considered to be sufficiently accurate at the time and are still commonly cited as benchmarks for validating numerical results in the recent numerical research works.

With recent advancement in computing technology, there is an increase in the adoption of numerical methods, especially Computational Fluid Dynamics (CFD), to investigate large and complex structures. Iwanowski *et al.* (1993) investigated the two-dimensional air cushion effect by coupling compressible viscous air and incompressible viscous water. Later, Korobkin (1996) took the effect of water compressibility into consideration when estimating the pressure distribution via acoustic approximation and normal modes, and the result showed the water compressibility has little influence on the slamming force. Fairlie-Clarke and Tveitnes (2008) simulated water entry of wedge-shaped sections with various deadrise angle ranging from 5° to 45°. Later in their experiments (Tveitnes *et al.*, 2008), their experimental results agreed well with the CFD results.

In relation to real engineering application, Næss *et al.* (2014) simulated a suction anchor crossing splash zone, the importance of entrapped air and water were particularly well presented by CFD method while they were hardly observed by the analytical or experimental methods. Swidan *et al.* (2014) simulated a free-falling wave-piercing catamaran model in the calm water to estimate the slamming load, its corresponding motions and flow visualisation. However, there is a lack of published work with regard to perforated plates.

In this study, the water entry process of perforated plates was modelled using the URANS equations and Volume of Fluid (VOF) method. Verification and validation of the numerical setup were achieved by comparing with experiments results (Campbell and Weynberg, 1980). The influences of various perforation ratios and layout configurations on the slamming coefficients were studied. In addition, this paper also examined the importance of air compressibility by modelling flat plate water entry.

2. NUMERICAL METHOD

2.1 BASIC GOVERNING EQUATIONS

The governing equations for the two-phase incompressible flow problem are given by the following equations (Jasak, 1996):

$$\frac{\partial \mathbf{u}}{\partial t} + \nabla(\mathbf{u}\mathbf{u}) = -\nabla p + \mathbf{g} + \nabla \cdot (\nu \nabla \mathbf{u}) \quad (1)$$

here, $\mathbf{u} = (u,v,w)$ is the velocity field in Cartesian coordinates, ∇ is $(\partial/\partial x, \partial/\partial y, \partial/\partial z)$, p represents the pressure, \mathbf{g} is the gravitational acceleration. ν is the kinematic viscosity. As the flow is effectively incompressible, then the continuity equation will be:

$$\nabla \cdot \mathbf{u} = 0 \quad (2)$$

When considering compressible gas, the continuity equations need to be solved with an additional energy equation together to predict the temperature. Therefore, the compressible Navier-Stokes equation and continuity equation will be given as follows:

$$\frac{\partial \rho \mathbf{u}}{\partial t} + \nabla \cdot [\rho \mathbf{u} \mathbf{u}] = \rho \mathbf{g} - \nabla (p + \frac{2}{3} \mu \nabla \cdot \mathbf{u}) + \nabla \cdot [\mu (\nabla \mathbf{u} + (\nabla \mathbf{u})^T)] \quad (3)$$

$$\frac{\partial \rho}{\partial t} + \nabla \cdot (\rho \mathbf{u}) = 0 \quad (4)$$

The energy equation is:

$$\frac{\partial \rho e}{\partial t} + \nabla \cdot [\rho e \mathbf{u}] = \rho \mathbf{g} \mathbf{u} - \nabla (p \mathbf{u} + \frac{2}{3} \mu (\nabla \cdot \mathbf{u}) \mathbf{u}) + \nabla \cdot [\mu (\nabla \mathbf{u} + (\nabla \mathbf{u})^T) \mathbf{u}] + \nabla \cdot (\lambda \nabla T) + \rho Q \quad (5)$$

where ρ is the density, μ is the dynamic molecular viscosity, e is the specific sensible energy, λ is the transport coefficient, T is the temperature and Q represents the volume energy sources. Also, for the laminar model, the terms which are associated with turbulence can be ignored (Larsen, 2013).

2.2 VOLUME OF FLUID (VOF) METHOD

VOF method is one of the well-known mesh-based methods to deal with the free surface. The volume fraction is defined below to describe the spatial distribution of each phase (CD-adapco, 2014):

$$\alpha_i = \frac{V_i}{V} \quad (6)$$

Only 2 phases are studies in this research, therefore the physical properties can be determined by volume fraction by following two equations:

$$\rho = \rho_{air} \alpha_{air} + \rho_{water} (1 - \alpha_{air}) \quad (7)$$

$$\mu = \mu_{air} \alpha_{air} + \mu_{water} (1 - \alpha_{air}) \quad (8)$$

The mass conservation equation describing the transport of volume fraction is:

$$\int_V \left(s_{\alpha_i} - \frac{\alpha_i}{\rho_i} \frac{D\rho_i}{Dt} \right) dV = \frac{\partial}{\partial t} \int_V \alpha_i dV + \int_S \alpha_i (\mathbf{v} - \mathbf{v}_g) \cdot \mathbf{n} da \quad (9)$$

here, s_{α_i} and $D\rho_i/Dt$ are the source of sink of each phase and the Lagrangian derivative of the phase density, respectively.

3. BENCHMARK CASE STUDY

Verification was performed to demonstrate the accuracy of the CFD model and gain confidence in numerical results. A benchmark study was first performed to simulate an experiment involving the water entry of a circular cylinder. The verification process focuses on the mesh independence study and time-step size independence study to estimate the numerical errors.

3.1 WATER ENTRY OF QUASI-CIRCULAR CYLINDER

To validate the proposed method, a circular cylinder with a radius of $R=10\text{cm}$ was simulated to come in contact with the free surface vertically at a speed of 5m/s . The results were compared with the experiment conducted by Campbell and Weynberg (1980).

The mesh quality and the computational domain are illustrated in Figure 1, whereby the information on the mesh (i.e. base size, G_B) is shown in Table 1. The refined mesh region around the cylinder with a cell size of $0.125G_B$ is considered to be sufficient in computing the water entry, especially at the region between cylinder bottom and the free surface. An anisotropic mesh was applied in the z direction at the free surface to capture wave deformation. The background domain was built with the consideration of the effect of the reflected wave and boundary conditions.

The cylinder was initially located 1cm above the free surface as shown in Figure 2. The bottom boundary was defined as a velocity inlet, to specify a velocity equal to the constant drop velocity of the case being modelled; and a pressure outlet was defined at the top of the domain. The left boundary was specified as symmetry plane to save computational resources, while the rest walls were defined as slip wall.

3.2 VERIFICATION AND VALIDATION

Verification and validation were conducted by following the generalised Richardson's Extrapolation method described by Wilson *et al.* (2001) and Stern *et al.* (2001). As shown in equations below, the numerical uncertainty U_{SN} is composed of iterative uncertainty U_I , grid uncertainty U_G and time-step uncertainty U_T .

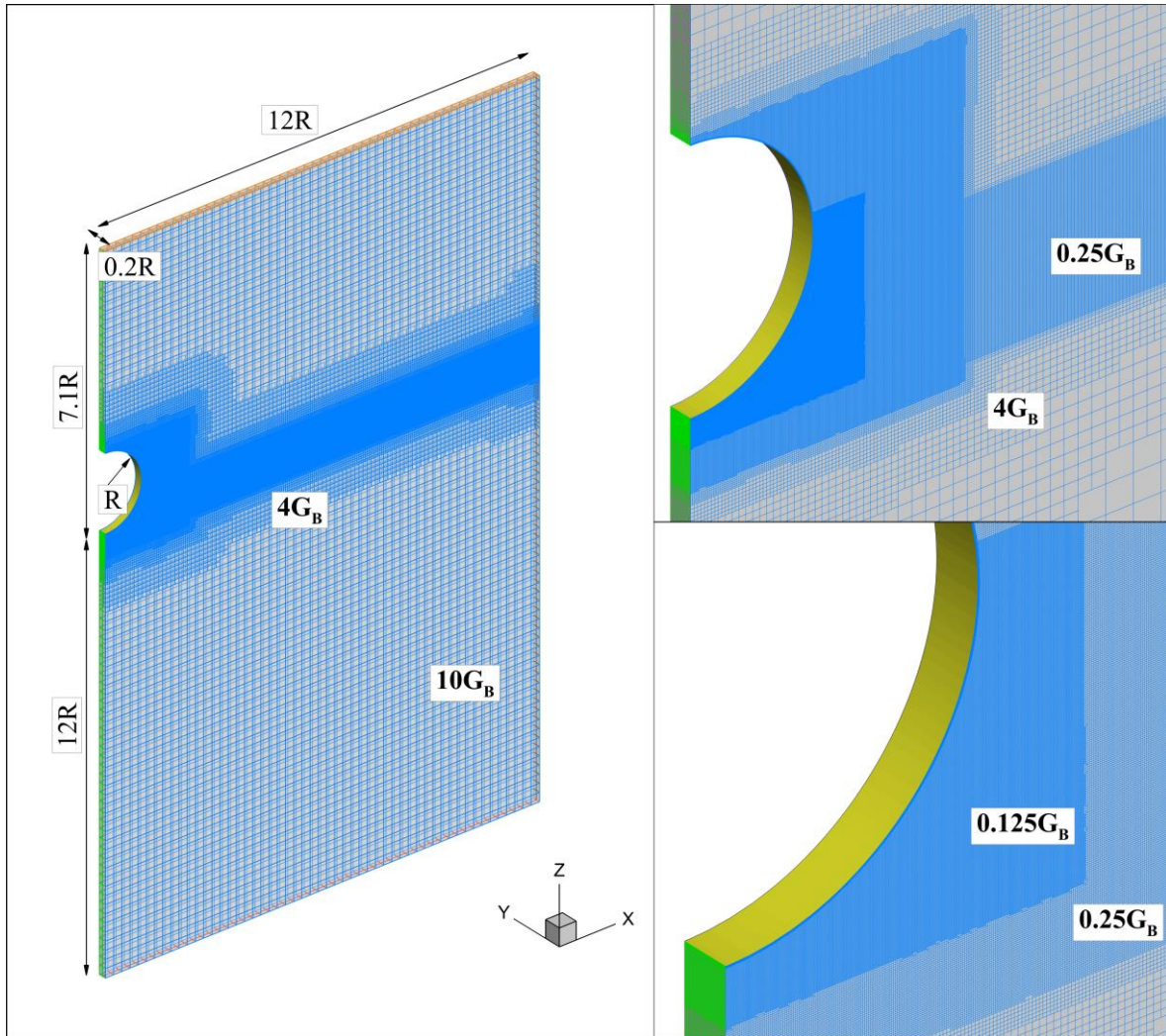


Figure 1: Illustration of computational domain and grid for water entry of cylinder

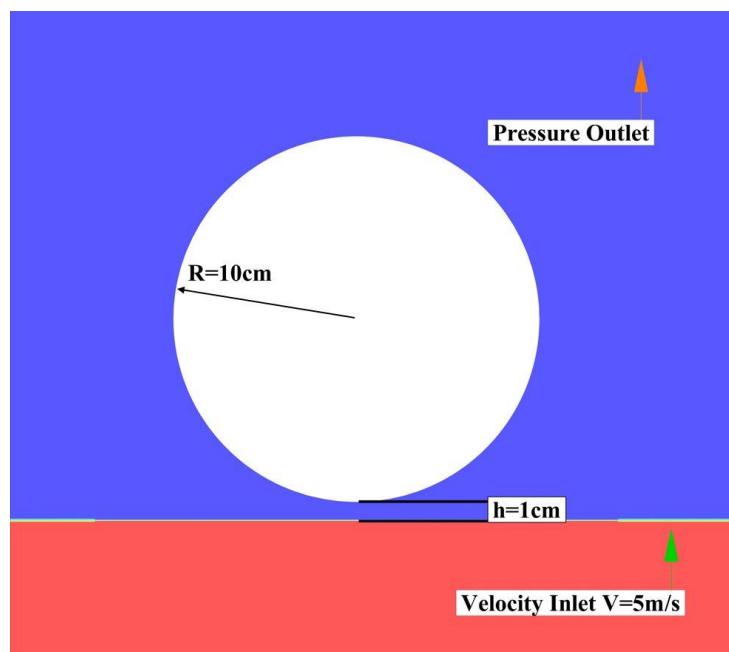


Figure 2: Initial location of cylinder

Table 1: Numerical simulation setup information

Case	Fine	Medium	Coarse
Base size G_B (mm)	2	2.828	4
Inner trimmer size (mm)	0.25	0.3536	0.5
Time step size (s)	6.25E-7	-	-
Grid cell number	19,626,083	7,375,210	2,774,724
	Small	Medium	Large
Base size G_B (mm)	2.828	-	-
Time step size (s)	1.5625E-07	3.125E-07	6.25E-7

The iterative uncertainty is neglected because all simulations have converged to result in a small magnitude, therefore, only the grid and time step convergence study are performed.

$$U_{SN}^2 = U_I^2 + U_G^2 + U_T^2 \quad (10)$$

With regards to the convergence studies, three different grid and time-step configurations were used with a refinement ratio, $r_k = \sqrt{2}$ and 2, respectively. Detailed configuration is given in Table 1 below. Solution variations should be assessed based on the differences between coarse-medium ($\varepsilon_{k32} = S_{k3} - S_{k2}$) and medium-fine ($\varepsilon_{k21} = S_{k2} - S_{k1}$) solutions as given below:

$$R_k = \varepsilon_{k21} / \varepsilon_{k32} \quad (11)$$

According to the R_k value, three convergence conditions are possible as follows:

- i. Monotonic convergence: $0 < R_k < 1$
- ii. Oscillation convergence: $R_k < 0$
- iii. Divergence: $R_k > 1$

For condition (iii), error and uncertainty cannot be estimated and therefore the simulation result is not valid; for condition (ii), the uncertainty is simply calculated based on the maximum oscillation solution S_U and S_L minimum oscillation solution as follows:

$$U_{ii} = 0.5(S_U - S_L) \quad (12)$$

For condition (i), the generalised Richardson's Extrapolation method can be used to calculate the numerical error and order of accuracy as shown below:

$$\delta_{RE_{k1}}^* = \frac{\varepsilon_{k21}}{r_k^{p_k} - 1} \quad (13)$$

$$p_k = \frac{\ln(\varepsilon_{k32} / \varepsilon_{k21})}{\ln(r_{k21})} \quad (14)$$

A correction factor is introduced to determine the proximity of the solutions to the asymptotic range and defined as follows:

$$C_k = \frac{r_k^{p_k} - 1}{r_k^{p_{kest}} - 1} \quad (15)$$

where p_{kest} is the limiting order of accuracy, based on the assumed theoretical order of accuracy or solutions for simplified geometry and conditions. If C_k is close to 1, it indicates that the solution is close to asymptotic range. Thus, the numerical error δ_{k1}^* , benchmark value S_c and the uncertainty U_{kc} / U_k can be estimated as follows:

$$\delta_{k1}^* = C_k \cdot \delta_{RE_{k1}}^* \quad (16)$$

$$S_c = S - \delta_{k1}^* \quad (17)$$

$$U_{kc} \begin{cases} \left[\left[2.4(1-C_k)^2 + 0.1 \right] \left| \delta_{RE_{k1}}^* \right|, |1-C_k| < 0.25 \\ \left[|1-C_k| \right] \left| \delta_{RE_{k1}}^* \right|, |1-C_k| \geq 0.25 \end{cases} \quad (18)$$

If the correction factor is away from unity, only the numerical uncertainty can be estimated:

$$U_k \begin{cases} \left[\left[9.6(1-C_k)^2 + 1.1 \right] \left| \delta_{RE_{k1}}^* \right|, |1-C_k| < 0.125 \\ \left[2|1-C_k| + 1 \right] \left| \delta_{RE_{k1}}^* \right|, |1-C_k| \geq 0.125 \end{cases} \quad (19)$$

The simulation results for grid and time-step conditions along with their uncertainties are listed in Table 2.

3.3 COMPUTATIONAL RESULTS

The slamming coefficient for the circular cylinder is predicted using Eq (20) and the results are compared with the experimental value as shown in Figure 3 and Figure 4.

$$C_S = \frac{2F_S}{\rho A_p v_S^2} \quad (20)$$

where F_S is the force acting on the object in vertical direction at the initial time, A_p is the project area of object normal to the direction of oscillation and v_s is the slamming impact velocity.

It can be observed from Figure 3 and Figure 4 that a large impulsive force occurs within a very short time (in the order of 200-250 μ s) when the bottom of the cylinder came in contact with the free surface. After the cylinder

penetrated the free surface, this force (directly proportional to the slamming coefficient) reduced rapidly to a small magnitude. The results also show that good spatial and temporal convergences were achieved since the differences in the results were very small. In addition, the computed free surface deformation exhibits a close correlation with that observed in the experiment conducted by Greenhow and Lin (1983) as shown in Figure 5. The uncertainty study and its results are listed in Table 2.

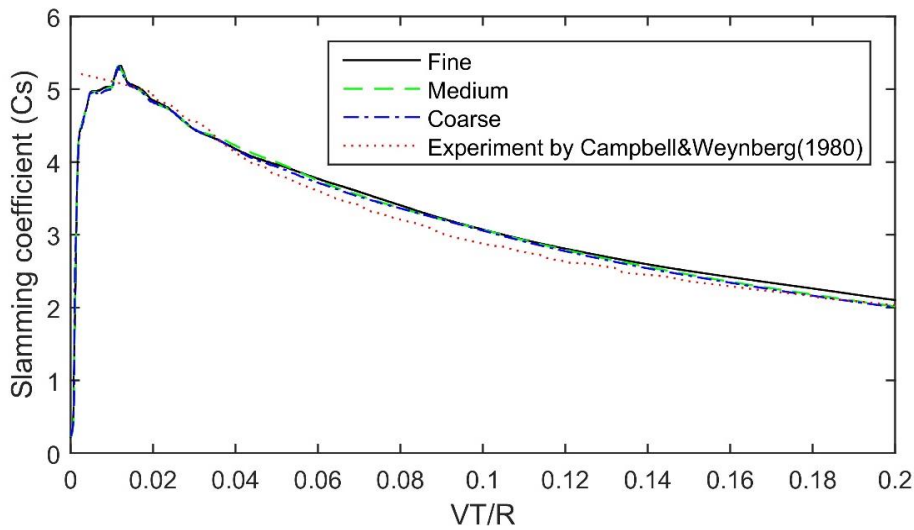


Figure 3: Slamming coefficient for three mesh sizes during initial water entry period

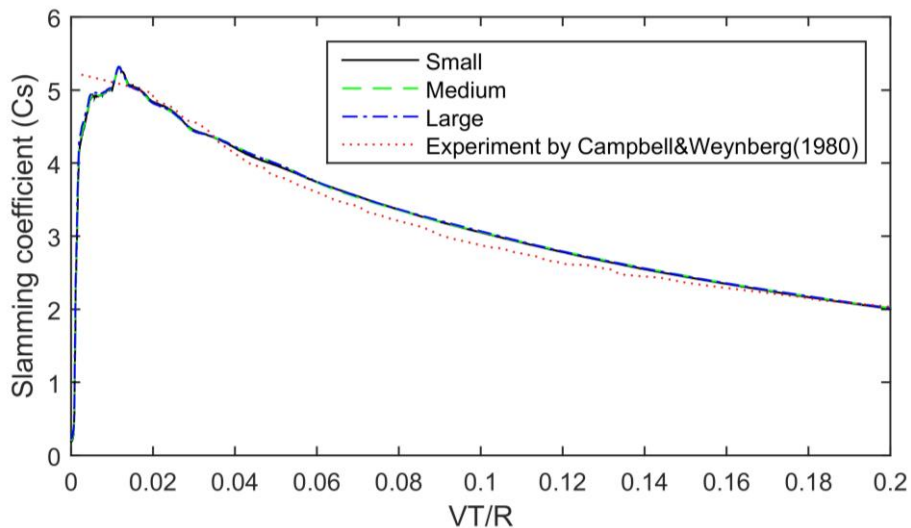


Figure 4: Slamming coefficient for three different time step sizes during initial water entry period

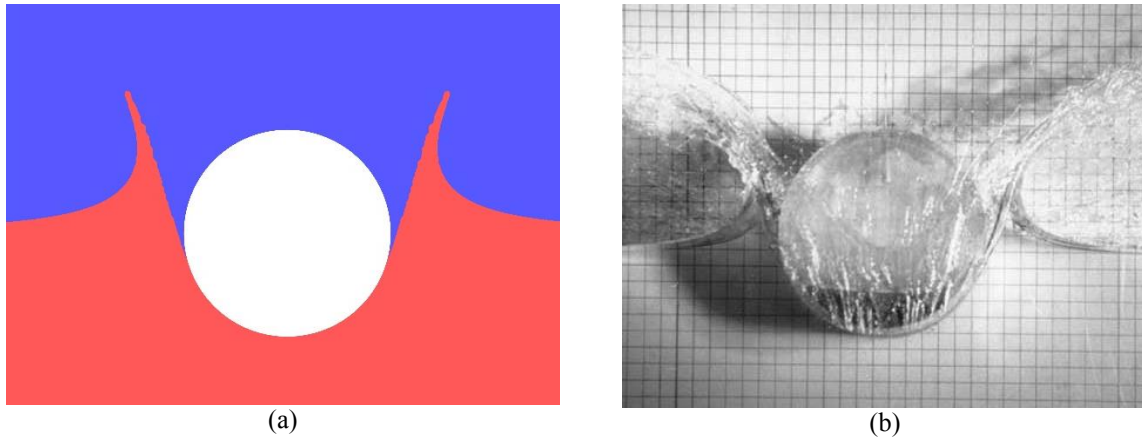


Figure 5: a) Numerical model (b) Experimental results by Greenhow and Lin (1983) at $t=0.330s$, almost $VT/R=1$, free drop

Table 2: Grid and time-step uncertainty study for circular cylinder

	r_k	Solution			R_k	U_{GC} / U_T	% S_1
		S_1	S_2	S_3			
Grid	$\sqrt{2}$	5.323	5.320	5.315	0.6	0.01	0.19
Time step	2	5.315	5.320	5.289	-0.6	0.0025	0.05

It can be seen from the results listed in Table 2, that the slamming coefficients of each configuration are very close. Therefore, both the estimated corrected grid uncertainty U_{GC} and time step uncertainty U_T are reasonably small, and their value (0.19% S_1 and 0.05% S_1) are considered to be acceptable. The difference between numerical and experiment values (Campbell and Weynberg, 1980) is small (i.e. 3.3%), which indicates that the slamming force will be well predicted if similar grid and time-step sizes were selected. Therefore, the numerical model is proven to have the ability to accurately predict the slamming force for the perforated plate.

4. SYSTEMATIC COMPUTATIONS

4.1 COMPUTATIONAL MATRIX

The geometries of two series of models are shown in Figure 6 and Figure 7 with key parameters listed in Table 3. The first series of models consist of perforated plates with different perforation ratios ranging from 0%, 20%, 30% to 40%. The second series of models are perforated plates with different layouts (i.e. gap numbers) with fixed ratio of 30%. All plates have the same external dimensions of 13m×10m×0.7m. The plate is positioned 0.1m above the free surface and dropped vertically with a constant velocity of 0.5m/s.

Uncertainty analysis was performed for Case 2 with the generalised Richardson’s Extrapolation using

systematically refined grid-spacing and time-steps, and Table 4 shows the calculated grid and time step uncertainties. Since $0 < R_k < 1$, the monotonic convergence can be confirmed by both two studies. The grid and time step uncertainties are small, and their values (6.3% S_1 & 11.5% S_1) are both considered to reasonably acceptable for three-dimensional simulations. It should be noted that, although further refinement of mesh size and/or time step size will produce a more accurate result and smaller uncertainties. However, the required computational resources will increase significantly. Therefore, from the resource point of view, it is sufficient to accept a reasonable solution by comparing with a quasi-two-dimensional simulation of the circular cylinder studied above with small variations.

4.2 INFLUENCE OF AIR COMPRESSIBILITY

The compressibility of air should be taken into account in terms of the flat plate without any gaps as the trapped air will be forced out from the underneath of the flat plate (Chuang, 1966, Faltinsen, 1990, Huera-Huarte et al., 2011). Therefore, Case 1 was investigated to examine the importance of air compressibility. The velocity contour of air is presented in Figure 8, before the flat plate came into contact with the free surface. It can be seen that the local air velocity has been accelerated to a value larger than 102m/s at the spray root, which translates to a Mach number that is greater than 0.3.

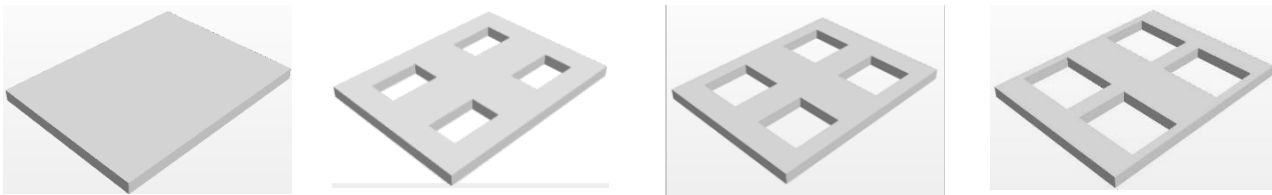


Figure 6: Perforated plates with varied perforation ratio, from left to right: 0%, 20%, 30% and 40%

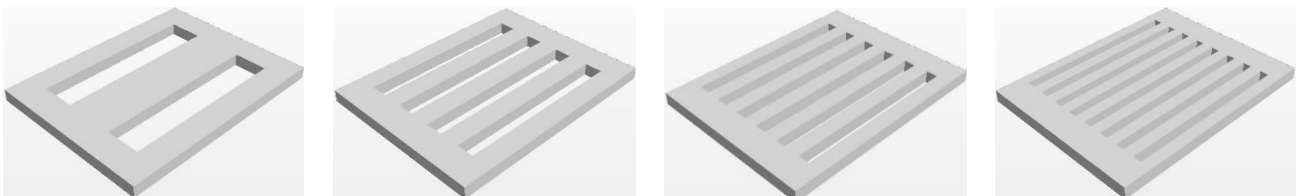


Figure 7: Varied layout configuration with fixed perforation ratio of (30%). From left to right: 2 gaps, 4 gaps, 6 gaps and 8 gaps

Table 3: Simulation cases for layout configuration and perforation ratio

Case no.	Perforation ratio (%)	Gap No.	Gap Length/Width Ratio
1	0	0	-
2	20	4	1.625
3	30	4	1.076
4	40	4	1.230
5	30	2	4.875
6	30	4	9.750
7	30	6	19.500
8	30	8	39.000

Table 4: Uncertainty study for Case 2

	r_k	Solution			R_k	U_{GC} / U_T	%S ₁
		Cs ₁	Cs ₂	Cs ₃			
Grid	$\sqrt{2}$	14.03	14.5	19.22	0.1	0.89	6.3
Time step	2	14.03	15.32	17.18	0.69	1.62	11.5

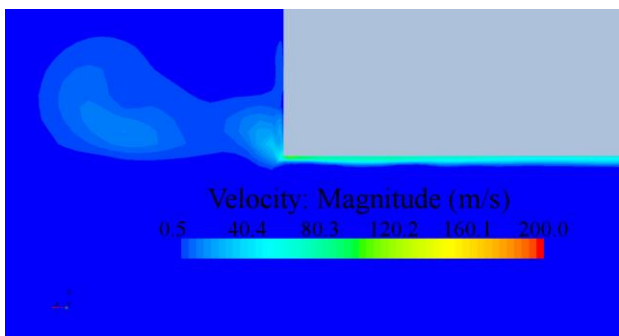


Figure 8: Front view of velocity contour at 0.11s before water entry, grey part represents the corner of the flat plate

Therefore, it is necessary to consider air compressibility when the air cushion is generated before the slamming impact for the flat plate (Anderson Jr, 2010). The slamming coefficients predicted by compressible and incompressible URANS equations are shown in Figure 10, respectively. It was found that the slamming coefficient was significantly reduced and the impact time was extended when the compressibility of air was considered. As shown in Figure 9, the free surface is deformed by the large air velocity and its pressure, some region is suppressed by the air cushion while other region is lifted up and accelerated to impact the bottom of the flat plate. This deformation leads to the occurrence of slamming impact in advance.

With reference to Figure 10 showing the time history of slamming coefficient, the compressible solver produced a negative force, which followed the maximum vertical force after the entire bottom surface of the flat plate had come in contact with the free surface. A similar result was also obtained by Huera-Huarte *et al.* (2011) in his experiments. This can be explained by the pressure contours in Figure 11, where a large low pressure zone occurred underneath the flat plate, thus, leading to a large downward force on the flat plate, when air compressibility was considered, while this phenomenon was absent without the consideration of air incompressibility.

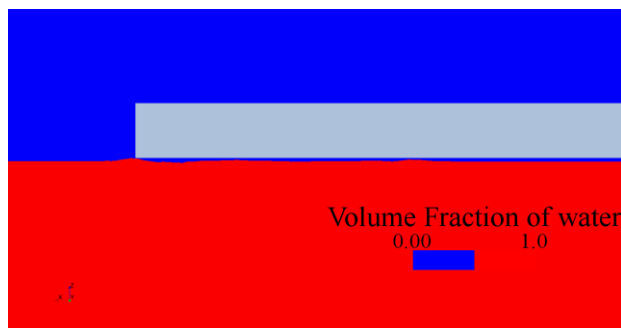


Figure 9: Front view of free surface deformation at 0.12s when flat plate came in contact with free surface

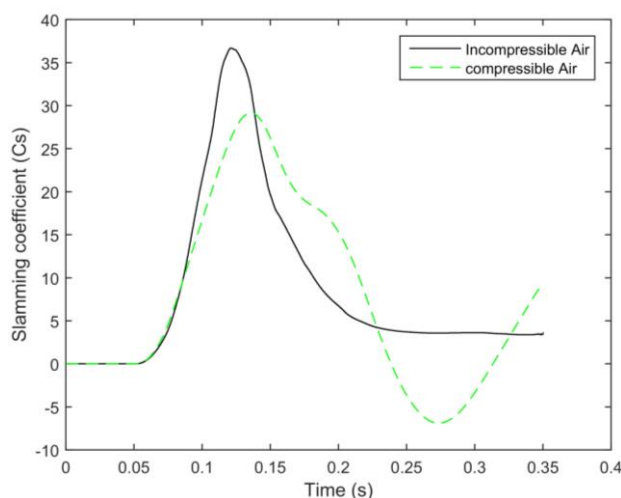
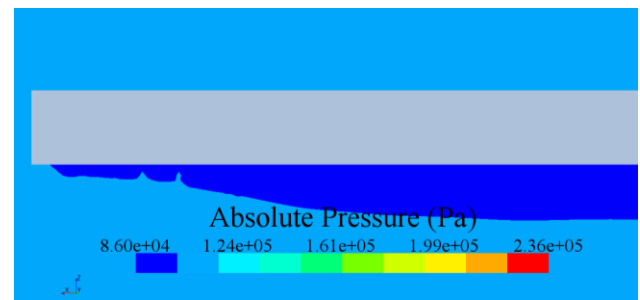
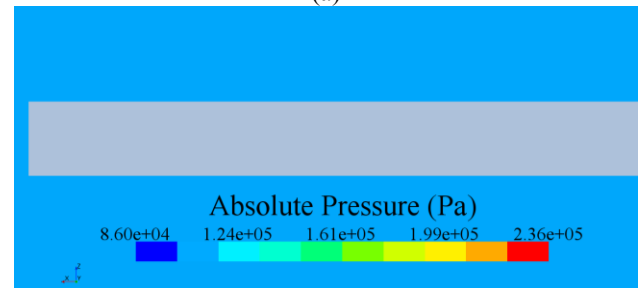


Figure 10: Time history of slamming coefficients of flat plate for compressible and incompressible air



(a)



(b)

Figure 11: Front view of pressure contour showing low pressure region during water entry at 0.26s, from top to bottom: (a) Compressible air, (b) incompressible air

4.3 INFLUENCE OF PERFORATION RATIO

The results of slamming coefficient predicted for different perforation ratios using the studied solver are shown in Figure 12. It can be seen that the slamming coefficient drops significantly from 29.0 at the ratio of 0% to 15.0 at the ratio of 20%, which demonstrates that the perforated structure has a great advantage in reducing the load on the hoisting line during lowering operation. Consequently, the slamming coefficient slightly decreases from 15.0 to 14.4 as shown in Figure 12. The differences among last three ratios (2.6% and 3.3%, respectively) are very small. The free surface deformation and water velocity are presented in Figure 13 and Figure 14, respectively. The plot presented in Figure 13 depicts the free surface deformation when the perforated plate came in contact with the free surface with trapped air. The contact location was found to be at the edge of the plate due to the uprise of water.

The vertical velocity of water underneath most of the plate was significantly suppressed as seen in Figure 14. While the velocity of water at the edge of the plate had a large value, indicating again that the trapped air accelerated the water nearby when it was trying to evacuate from the edge and gaps. However, by comparing the vertical velocity of the free surface, on the bottom surface of the flat plate in Figure 14 (a) with that of perforated plates in Figure 14 (b)-(d), it was found that vertical velocity of the free surface near the four edges of flat plate was accelerated and much higher than the other plates in the same locations. Therefore, the estimated slamming coefficient value for the flat plate is much larger than

that for the perforated plates as shown in Figure 12. In addition, the velocity contours of three different perforated plates presented in Figure 14 (b)-(d) are similar which indicates that the ability of the trapped air to escape through the gaps and edges between the

bottom of the plate and free surface, is comparable to each other. Therefore, the slamming coefficients of different ratios are very close to each other, if the gap is not slender in shape (length/width ratio smaller than 1.625).

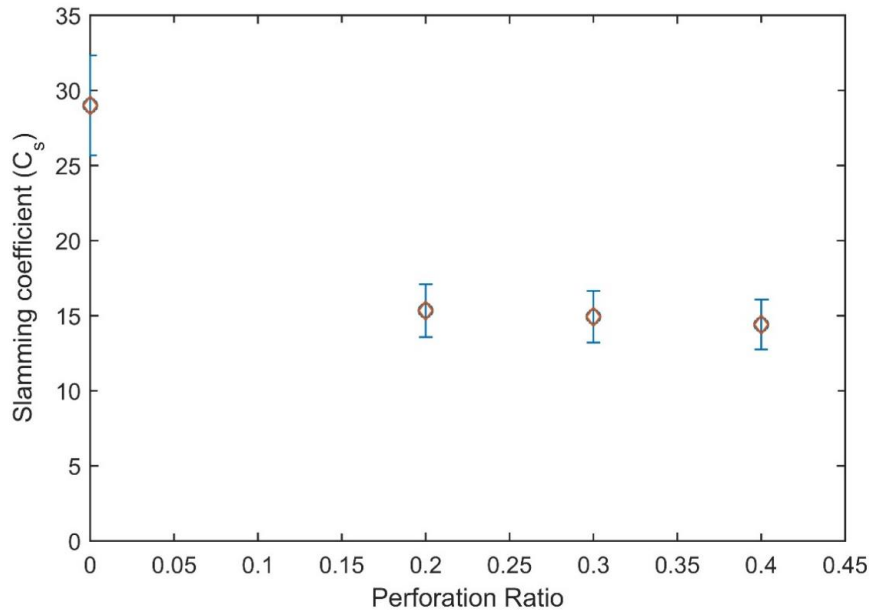


Figure 12: Slamming coefficient of different perforation ratios on fixed layout configuration

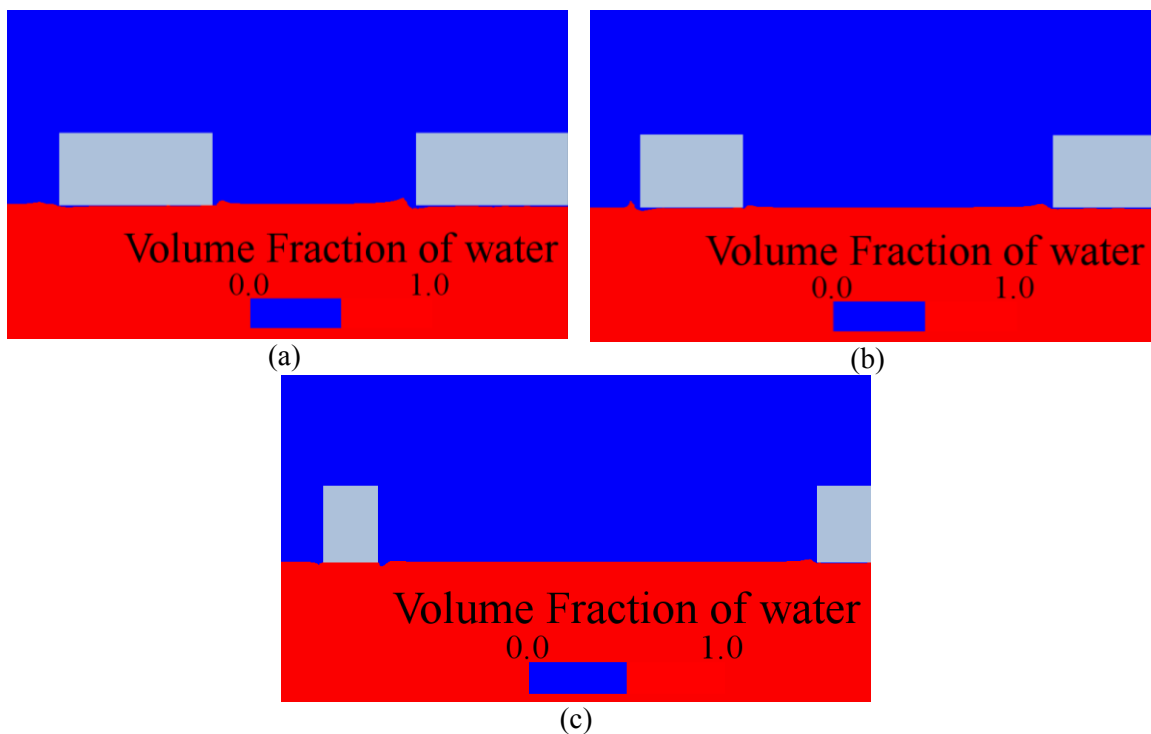


Figure 13: Front view of free surface deformation with respect to different ratios at 0.2s, constant $y=3.25m$: (a) 20%; (b) 30%; (c) 40%

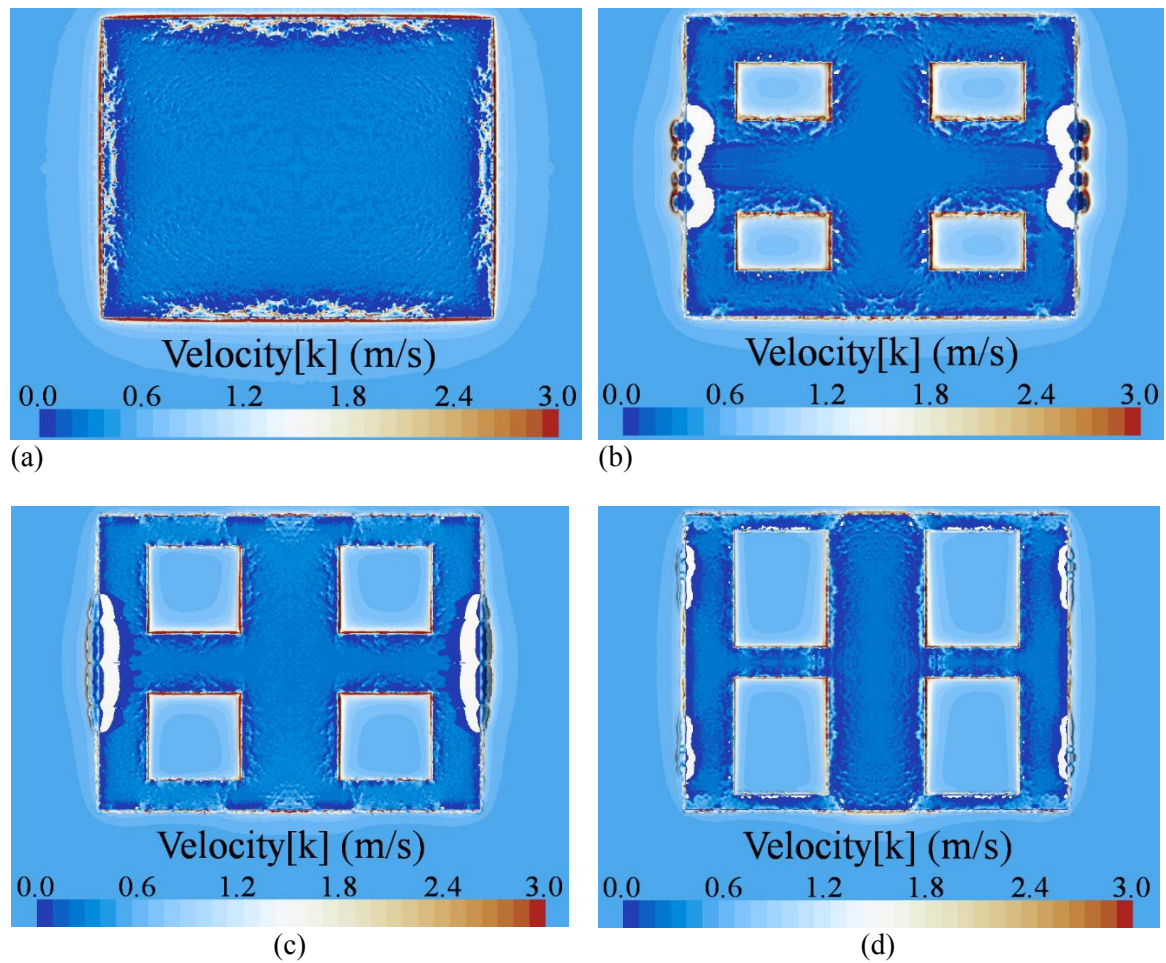


Figure 14: Contour plots of free surface velocity distribution with respect to different ratios at 0.2s: (a) 0%; (b) 20%, (c) 30%; (d) 40%

4.4 INFLUENCE OF GAP LAYOUT CONFIGURATION

The second series of water entry of plates with different layout configuration were simulated as given in Figure 7. As shown in Figure 15, the slamming coefficient increases linearly from 9.7 to 11.3 along with the increase of gap numbers with fixed perforation ratio until 6 gaps layout. Thereafter, the slamming coefficient reduces from 11.3 at 6 gaps to 8.6 at 8 gaps, where the magnitude of reduction rate is 24%. To explain this trend, the corresponded free surface deformations are plotted in Figure 16. The free surface elevations were compared to illustrate the change in slamming coefficient for different gap configurations. It can be seen that there is less interference between plate edge and water in Figure 16 (d), indicating that different layout configurations have a significant impact on the free surface deformation. The free surface contour plots also demonstrate that the air underneath the plate is trying to escape through the gaps and edge as discussed in the

previous section. In addition, the reduction in the slamming coefficient for the case of the 8-gaps layout can be explained based on Figure 17. A large low pressure area can be seen under the gaps as compared to the 6-gaps configuration. It is suggested that a large air group isolates the water-plate interaction which leads to a smaller force due to the presence of this low pressure region. Therefore, a conclusion can be made, whereby for a fixed perforated ratio, the slamming coefficient will increase with the increase in length/width ratio until it reaches 19.5. However, a further increase in length/width ratio may impose a negative impact on the air escape due to the increase in gap number. Combining with Figure 18, which shows the vertical velocity of the free surface. The water velocity is clearly suppressed below 0.5m/s for all four layouts, which will lead to less water-plate interaction and a lower pressure. This highlights the importance of the air cushion effect. Additionally, the contact location was seen to shift from the edge of the perforated plate to the middle of the gaps with the increase in gap number.

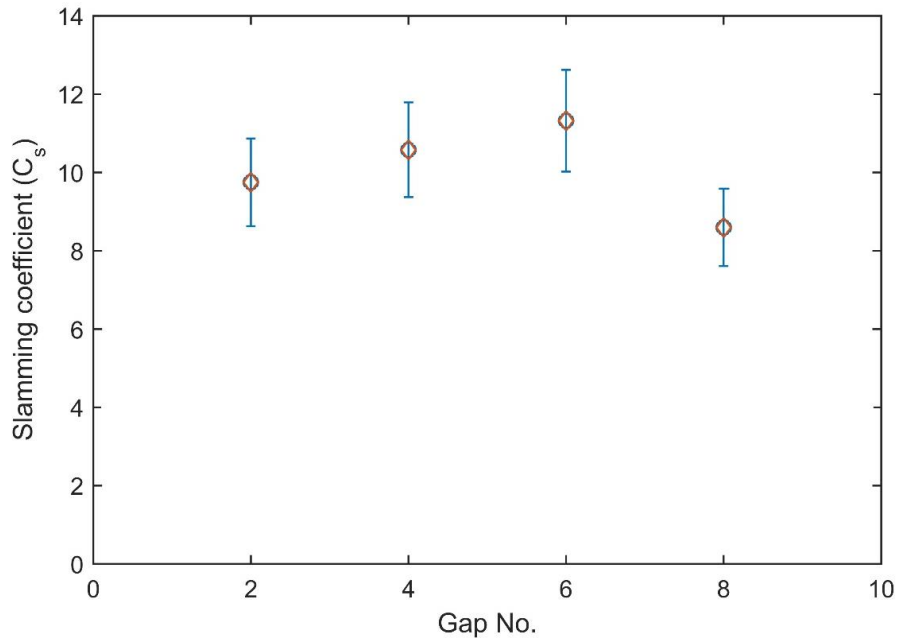


Figure 15: Slamming coefficient of different plate layout configurations on fixed perforation ratio

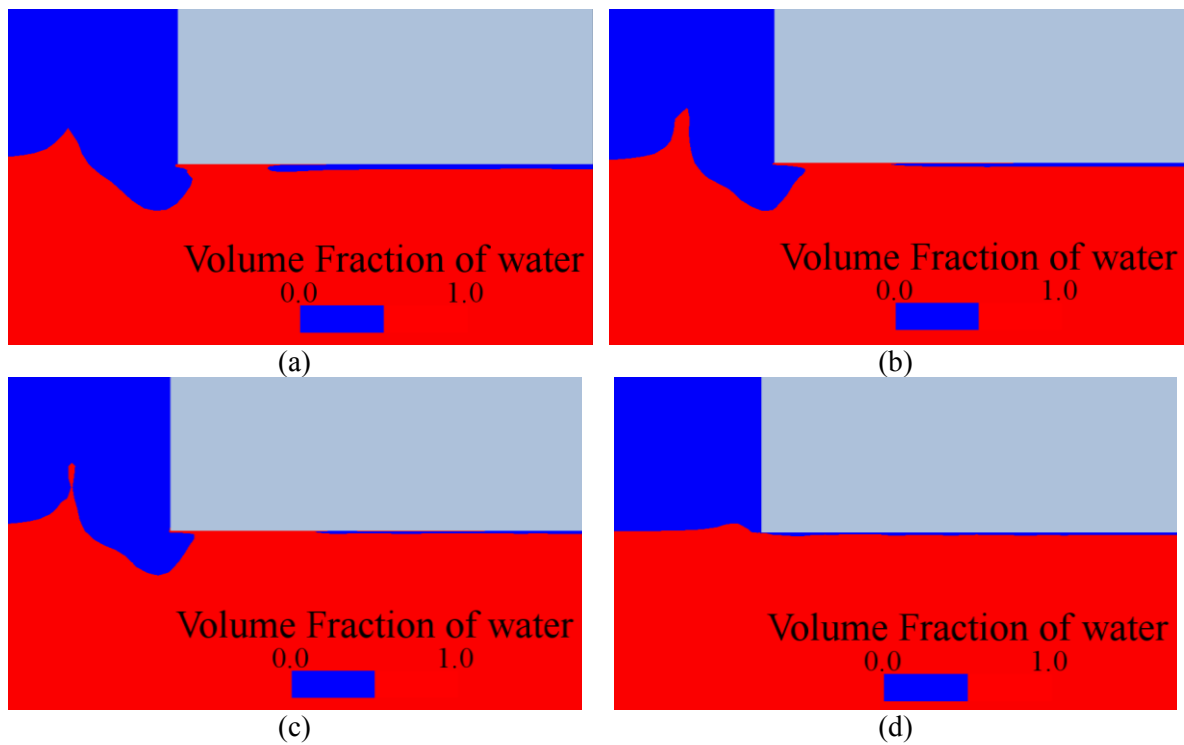


Figure 16: Front view of free surface deformation with respect to different gap configurations at 0.2s: (a) 2 gaps; (b) 4 gaps; (c) 6 gaps; (d) 8 gaps

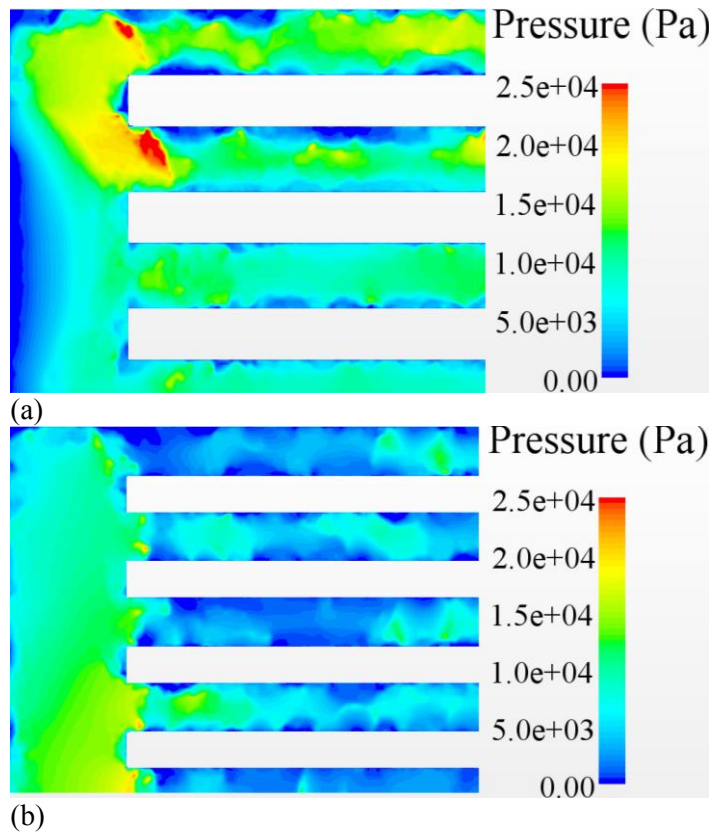


Figure 17: Quarter bottom peak pressure distribution contours with respect to 2 gap configurations: (a) 6 gaps; (b) 8 gaps

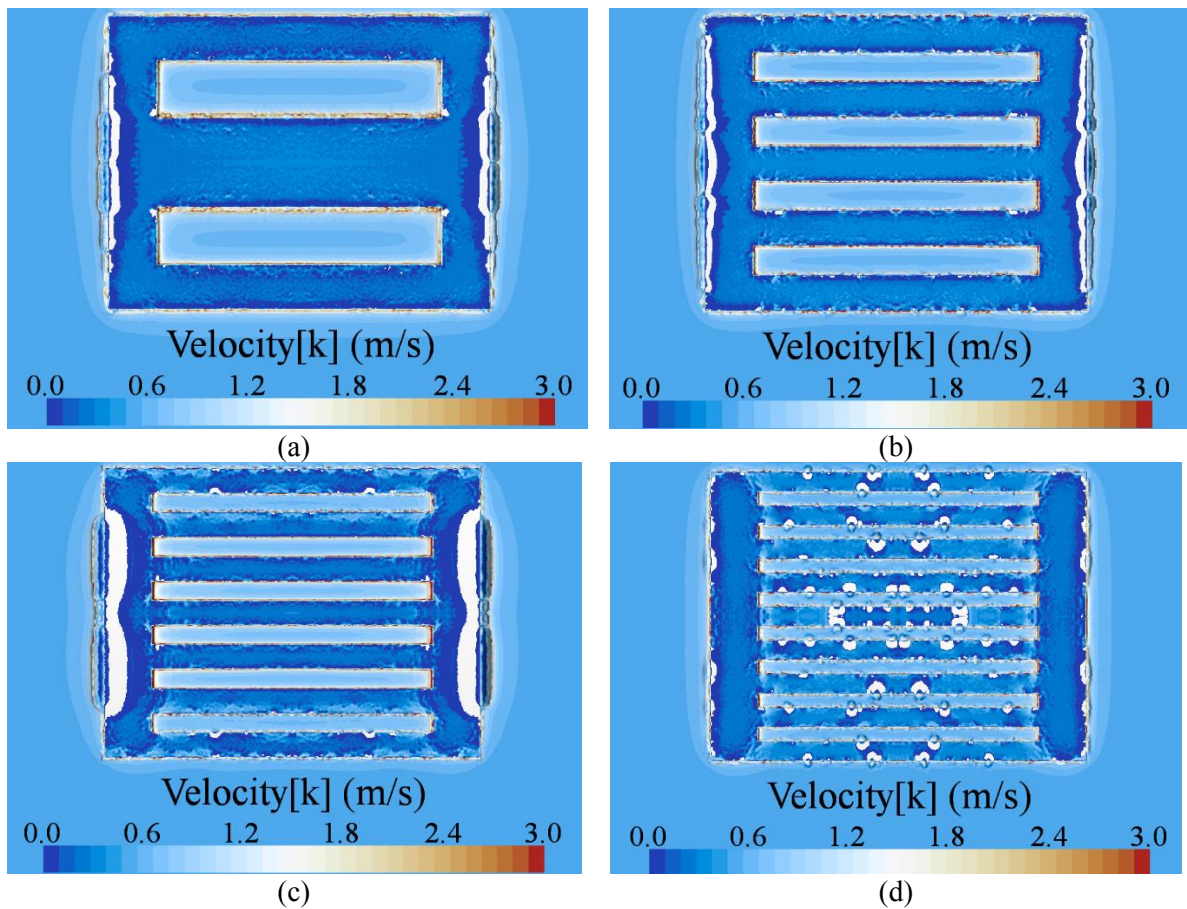


Figure 18: Contour plots of free surface velocity distribution with respect to different gap configurations at 0.2s: (a) 2 gaps; (b) 4 gaps; (c) 6 gaps; (d) 8 gaps

5. CONCLUSIONS

The water entry and slamming coefficients of perforated plates with different ratios and layout configurations were studied and reported in this paper using CFD. The numerical model was verified and validated by simulating a benchmark experiment for water entry of a circular cylinder (Campbell and Weynberg, 1980). From the benchmark study, a large impulsive force occurs within a very short time was found, when the bottom of the cylinder came into contact with the free surface. Besides this, the time history of slamming coefficient agreed well with the experiment value. In addition, the computed free surface deformation exhibited a close correlation with that observed in the experiment, indicating that numerical model can be used for prediction of slamming force.

Upon studying different plates with various perforated ratios and layout configurations, the following conclusions can be drawn:

- The slamming force was significantly reduced and the impact time is extended when the compressibility of air was considered by studying water entry of flat plate.
- For perforated plate with different ratios, if the gap had a small length/width ratio (smaller than 1.625), the ability of the trapped air to evacuate between the bottom of the plate and free surface through gaps was similar.
- For perforated plates with different layout configurations, the slamming coefficient increased with the increase in length/width ratio until it reached 19.5. However, a further increase in length/width ratio may impose a negative impact on the escape of air due to the increase of gap number.
- The series of simulations showed that the URANS equations and VOF method had the ability to model the water entry of large and complex subsea structures.

6. ACKNOWLEDGEMENTS

The authors acknowledge the computational resources cluster13 provided by the Australian Maritime College and High-performance computing (HPC) system provided by the TPAC, the University of Tasmania in the present work. The author would like to thank Mr Jun Yi Lee, the PhD candidate in Australian Maritime College for his selfless help.

7. REFERENCES

1. ANDERSON JR, J. D. 2010. *Fundamentals of aerodynamics*, Tata McGraw-Hill Education.
2. CAMPBELL, I. & WEYNBERG, P. 1980. *Measurement of parameters affecting slamming*.

3. CD-ADAPCO 2014. *User guide StarCCM+ version 9.02*.
4. CHUANG, S.-L. 1966. *Experiments on flat-bottom slamming*. Journal of Ship Research, 10, 10-17.
5. CHUANG, S.-L. 1970. *Investigation of impact of rigid and elastic bodies with water*. DTIC Document.
6. DNV 2011. Recommended Practice DNV_RP-H103. *Modelling and analysis of marine operations*.
7. FAIRLIE-CLARKE, A. & TVEITNES, T. 2008. *Momentum and gravity effects during the constant velocity water entry of wedge-shaped sections*. Ocean Engineering, 35, 706-716.
8. FALTINSEN, O. M. 1990. *Sea loads on ships and offshore structures*, UK, Cambridge University Press.
9. GREENHOW, M. & LIN, W.-M. 1983. *Nonlinear-free surface effects: experiments and theory*. DTIC Document.
10. HUERA-HUARTE, F., JEON, D. & GHARIB, M. 2011. *Experimental investigation of water slamming loads on panels*. Ocean Engineering, 38, 1347-1355.
11. IWANOWSKI, B., FUJIKUBO, M. & YAO, T. 1993. *Analysis of horizontal water impact of a rigid body with the air cushion effect*. Proceedings of Japan Shipbuilding Society 1993, 293-302.
12. JASAK, H. 1996. *Error analysis and estimation for finite volume method with applications to fluid flow*.
13. KOROBKIN, A. 1996. *Acoustic approximation in the slamming problem*. Journal of Fluid Mechanics, 318, 165-188.
14. LASRSEN, E. 2013. *Impact loads on circular cylinders*. Master Norwegian university of science and technology.
15. NÆSS, T., HAVN, J. & SOLAAS, F. 2014. *On the importance of slamming during installation of structures with large suction anchors*. Ocean Engineering, 89, 13.
16. STERN, F., WILSON, R. V., COLEMAN, H. W. & PATERSON, E. G. 2001. *Comprehensive approach to verification and validation of CFD simulations - part 1: methodology and procedures*. Journal of fluids engineering, 123, 793-802.
17. SWIDAN, A. A., THOMAS, G. A., AMIN, W., RANMUTHUGALA, D. & PENESIS, I. *Numerical investigation of water slamming loads on wave-piercing catamaran hull model*. 10th High speed marine vehicles Symposium, 2014. 1-9.
18. TVEITNES, T., FAIRLIE-CLARKE, A. & VARYANI, K. 2008. *An experimental investigation into the constant velocity water entry of wedge-shaped sections*. Ocean Engineering, 35, 1463-1478.

19. VERHAGEN, J. 1967. *The impact of a flat plate on a water surface*. J. Ship Res, 11, 211-223.
20. VON KARMAN, T. 1929. *The impact on seaplane floats during landing*.
21. WAGNER, H. 1932. *Über Stoß- und Gleitvorgänge an der Oberfläche von Flüssigkeiten*. ZAMM-Journal of Applied Mathematics and Mechanics/Zeitschrift für Angewandte Mathematik und Mechanik, 12, 193-215.
22. WILSON, R. V., STERN, F., COLEMAN, H. W. & PATERSON, E. G. 2001. *Comprehensive approach to verification and validation of CFD simulations—Part 2: Application for RANS simulation of a cargo/container ship*. Journal of Fluids Engineering, 123, 803-810.